SCIENTIFIC REPORTS
nature research

OPEN

Coupled Charge Transfer Dynamics and Photoluminescence Quenching in Monolayer MoS_2 Decorated with WS_2 Quantum Dots

Larionette P. L. Mawlong[1], Abhilasha Bora[2] & P. K. Giri[1,2*]

Herein, we have investigated the tunability of the photoluminescence (PL) of the monolayer MoS_2 (1L-MoS_2) by decorating it with WS_2 quantum dots (WS_2 QD). The direct bandgap 1L-MoS_2 and WS_2 QDs are grown by chemical vapor deposition and liquid exfoliation methods, respectively. The room temperature PL spectrum of bare 1L-MoS_2 is systematically quenched with its decoration with WS_2 QDs at different concentrations. A decrease in the work function of 1L-MoS_2 with the decoration of WS_2 QDs was established from the Kelvin probe force microscopy analysis. A detailed quantitative analysis using the four-energy level model involving coupled charge transfer was employed to explain the redshift and the systematic decrease in the intensity of the PL peak in 1L-MoS_2/WS_2 QD heterostructure. The modulation of the PL in the heterostructure is attributed to the increase in the formation of negative trions through the charge transfer from WS_2 QD to the 1L-MoS_2 and thus making the 1L-MoS_2 heavily n-type doped, with increase in the electron density by ~1.5×10^{13} cm^{-2}. This study establishes the contribution of defects in the coupled charge transfer dynamics in 1L-MoS_2, and it lays out a convenient strategy to manipulate the optical and electrical properties of 1L-MoS_2 for various optoelectronic applications.

The monolayer transition metal dichalcogenides TMDs (e.g., MoS_2, WS_2, $MoSe_2$, WSe_2, etc.) have drawn great attention for their fascinating properties and diverse range of applications, such as transistors[1,2], photodetectors[2–4], light-emitting devices[5], and sensors[6]. The strong Coulomb interactions in the atomically thin two dimensional materials create stable excitonic states even at room temperature[7,8]. Among most investigated 2D TMDs, monolayer MoS_2 (1L-MoS_2) has attracted significant attention due to its abundance in nature, tunable optical band gap, high chemical stability and efficient carrier generation[7–10]. An effective and convenient method to tune the optical properties of MoS_2 is to control the charge density. To induce charge transfer to/from the 1L-MoS_2, numerous methods were used such as chemical doping[11,12], plasmonic hot-electron doping[13], and electrical doping[14,15]. In the field-effect transistors (FET), application of gate bias voltage has been used to tune the charge density in the MoS_2, however, the complex device structure fabricated on the MoS_2 can lead to the non-uniform charge distribution and thus alter the optical measurement. Alternatively, gas molecules have also been used for carrier doping, but this method requires accurate control of the gas flow and its doping efficiency is reliant on the defect density of the material. Construction of hybrid architectures with MoS_2 is favorable due to the excitonic nature of optical excitations in its monolayer form. Interfacing 1L-MoS_2 with zero-dimensional semiconductor nanocrystal, also known as quantum dots (QDs) is one of the possible ways to control the optical properties of 1L-MoS_2. The QDs have remarkable properties such as strong absorption, size-dependent energy bandgap, and high-photoluminescence. In case of a hybrid 0D/2D structure, the absorptive properties of monolayer TMD are enhanced by the QD donors which improve the optoelectronic devices, producing more efficient photodetectors and solar cells. TMD QDs such as WS_2 QDs have gained wide interest due to their high solubility in both aqueous and non-aqueous solvents, good electrical conductivity and flexible to hybridize with other nanomaterials. Therefore, this material is highly promising for a wide range of applications. In a previous study, Li *et al.*[16] fabricated graphene QDs/1L-MoS_2 heterostructure (HS) and demonstrated charge transfer from graphene QDs to the 1L-MoS_2. This charge transfer at the interface between the QD and the 1L-MoS_2 induces competition between

[1]Centre for Nanotechnology, Indian Institute of Technology Guwahati, Guwahati, 781039, India. [2]Department of Physics, Indian Institute of Technology Guwahati, Guwahati, 781039, India. *email: giri@iitg.ac.in

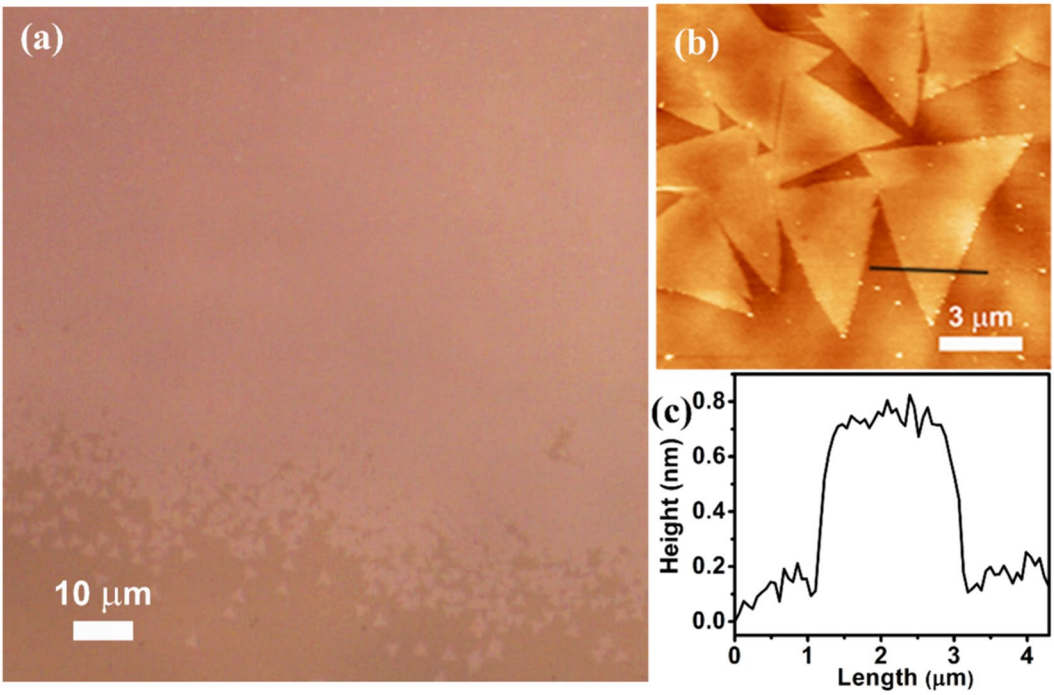

Figure 1. (**a**) Optical microscope image of large area monolayer MoS_2 grown on sapphire substrate. (**b**) AFM image of triangular shaped monolayer MoS_2 on sapphire substrate, and (**c**) AFM height profile taken along the black line in (**b**) showing a step height of ~0.7 nm confirming the monolayer MoS_2 growth.

neutral exciton and charged exciton (trion) population resulting in the modulation in the photoluminescence (PL) of 1L-MoS_2. Similarly, Roy *et al.*[17] fabricated a heterostructure composed of $MoSe_2$ QDs and 1L-MoS_2 or WSe_2 and studied the charge transfer mechanism. However, in these studies, the role of defects in PL quenching of the 1L-MoS_2 has not been addressed. To our knowledge, there is no report on the charge transfer from WS_2 QDs to 1L-MoS_2 and the resulting doping and PL quenching effect. It is interesting to study the role of defects in the charge transfer dynamics in the 1L-MoS_2 layers through PL spectroscopy and its implications for future applications. In the literature, the studies on heterostructures have been usually performed on chemically grown 2D layers, which are often multilayered and crystalline quality of layer is inferior to that grown by chemical vapor deposition (CVD) techniques.

Herein, we report a study on the tunability of the PL emission spectrum through charge transfer at the 1L-MoS_2/WS_2 QD HS interface. The HS was synthesized by WS_2 QDs prepared by the liquid exfoliation method onto the CVD grown 1L-MoS_2. The PL intensity of 1L-MoS_2 is reduced after the formation of the 1L-MoS_2/WS_2 QD HS. This quenching of the PL is traced to the charge transfer from the WS_2 QD to 1L-MoS_2 resulting in the conversion of the neutral exciton to trion, thus making the 1L-MoS_2 n-type doped. Additionally, the presence of defects may be another dominant factor that alters the PL emission. We show that by solving the carrier dynamics based on the coupled rate equations, we can have a better understanding of the contribution of the defects in the recombination dynamics of the hybrid structure.

Results and Discussion

Morphology studies. Figure 1(a) displays the optical image of monolayer MoS_2 film grown with triangular-shaped MoS_2 grains towards the edge of the sapphire substrate. These triangular shaped MoS_2 regions merge to form a large continuous monolayer film with millimeter-scale uniformity, as evident from Fig. 1(a). The layer uniformity is evident from the small difference in contrast over the whole film. Details of the growth conditions for monolayer MoS_2 film over a large area have been discussed in our previous work[18]. Figure 1(b) shows the AFM image of the triangular-shaped monolayer MoS_2. It reveals that the triangular-shaped MoS_2 have a tendency to interconnect with each other rather than overlap when they grow to form a continuous film as seen by the homogeneous color contrast, which further indicates a good uniformity. The AFM height profile taken along the black line in Fig. 1(c) indicates a thickness of ~0.7 nm, which corresponds to monolayer thickness. The AFM image of the 1L-MoS_2/WS_2 QD HS is shown in Fig. S1(a) (Supporting Information). The height profile of MoS_2 layer and the QDs decorated over it clearly revealed the growth of monolayer MoS_2 and monolayer WS_2 QDs, as shown in Fig S1(b) (Supporting Information).

The typical morphological and structural properties of the as-prepared WS_2 QDs were studied using TEM. Figure 2(a) shows the TEM image of the WS_2 QDs. The selected area electron diffraction (SAED) pattern (top right inset of Fig. 2(a)) shows the presence of diffused rings, which indicates the polycrystalline nature of the QD. The WS_2 QDs size ranges from 3–11 nm with an average diameter of 4.5 ± 0.2 nm, as shown in Fig. 2(b). The high-resolution TEM (HRTEM) image of the WS_2 QD (Fig. 2 (c)) displays ordered lattice fringes. The inset

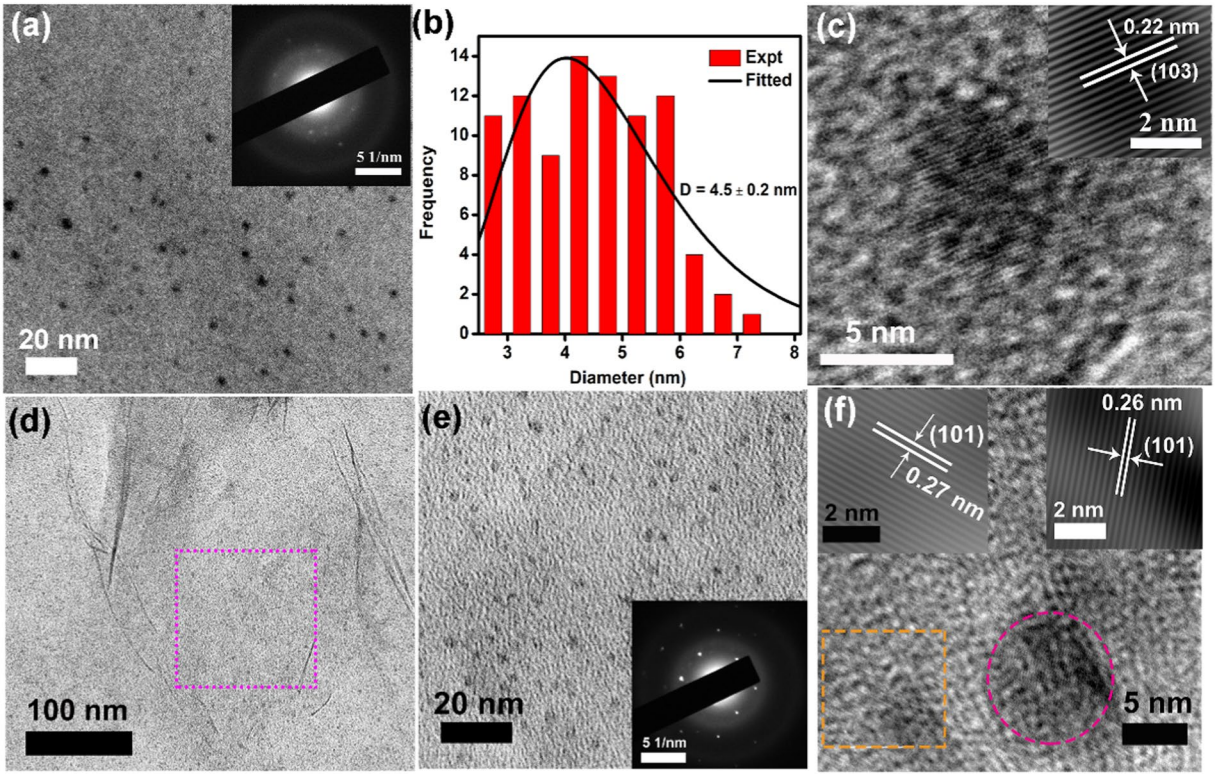

Figure 2. (**a**) The TEM image of WS_2 QDs; (**b**) the size distribution of QDs with an average size of 4.5 ± 0.2 nm; (**c**) HRTEM lattice image of a WS_2 QD; the inset shows the IFFT image of WS_2 lattice planes. (**d**,**e**) The TEM images of uniform decoration of WS_2 QDs on the 1L-MoS_2 at different magnifications. The inset of 2(**e**) shows the SAED pattern with hexagonally aligned diffraction spots (for 1L-MoS_2) and diffused rings (for WS_2 QDs). (**f**) HRTEM lattice fringe pattern of 1L-MoS_2/WS_2 QDs HS. The top-left inset is the IFFT image of the region enclosed by the dotted square showing the planes corresponding to MoS_2. The top-right inset shows the IFFT image of the area inside the dotted circle displaying the lattice fringe pattern of a WS_2 QD.

in Fig. 2(c) shows the inverse fast Fourier transform (IFFT) of the lattice fringes with an interplanar spacing of 0.22 nm, which corresponds to the (103) plane of WS_2. To examine the coverage of the WS_2 QDs on the 1L-MoS_2, TEM imaging of the 1L-MoS_2/WS_2 QD HS was carried out. Figure 2(d) shows a low magnification TEM image of the QD decorated on large area 1L-MoS_2 film. A higher magnification TEM image is depicted in Fig. 2(e), where a uniform surface coverage of WS_2 QDs is clearly observed over the MoS_2 layer. The corresponding SAED pattern shows the polycrystallinity of the WS_2 QDs. In addition, hexagonally aligned diffraction spots are attributed to the (101) plane of MoS_2 (inset of Fig. 2(e)). Thus, the as-grown 1L-MoS_2 is highly crystalline in nature and is uniformly decorated with WS_2 QDs. The HRTEM image of the 1L-MoS_2/WS_2 QD HS is displayed in Fig. 2(f), which shows distinct lattice planes. The top-left inset shows the IFFT of the atomic planes of the MoS_2 film. The lattice d-spacing is 0.27 nm that corresponds to (101) plane of MoS_2. Additional ordered domains are observed with a lattice spacing of 0.22 nm, which can be assigned to the (101) plane of WS_2 (top right inset of Fig. 2(f)).

Structural and optical analysis. The chemical composition of the 1L-MoS_2 and WS_2 QDs was confirmed from the XPS analysis. Figure 3 shows the XPS spectra of the core level Mo 3d, W 4 f and S 2p bands for the 1L-MoS_2 and WS_2 QDs samples. Figure 3(a) confirms the elemental composition of 1L-MoS_2 with the presence of the peaks of Mo and S. In Fig. 3(b), several Mo $3d_{5/2}$ and $3d_{3/2}$ peaks fitted for Mo (3d) envelope, indicating that more than one Mo species were present. The first peak, centered at 226.4 eV, agrees well with that of the 2 s binding energy of elemental S. The strongest Mo 3d doublet peaks for 1L-MoS_2 detected at 229.1 eV ($3d_{5/2}$) and 232.0 eV ($3d_{3/2}$) correspond to the +4 oxidation state of Mo, confirming the formation of MoS_2[19]. Additional Mo peaks were observed at 232.8 eV and 235.2 eV corresponding to the oxides of Mo metal (Mo^{6+}) probably due to the presence of traces of MoO_3 in the sample after CVD growth and post-synthesis exposure to air. Figure 3(c) exhibits the S 2p XPS spectra of 1L-MoS_2 with peaks at ~161.8 eV (S $2p_{3/2}$) and ~162.9 eV (S $2p_{1/2}$) corresponding to the divalent sulfide ions (S^{2-}). Additionally, a peak at 162.1 eV (S $2p_{3/2}$) (with 8.1% spectral weight) is present that could be due to the presence of surface defects introduced during the CVD growth. These defect sites are the S vacancies as there are fewer S atoms around the Mo atoms at such sites[20]. The survey scan XPS spectrum of WS_2 QDs shows the presence of W, S, C, N and O peaks (Fig. 3(d)). The high-resolution XPS spectrum for carbon (C 1 s) is shown in Fig. S2 (Supporting Information). The deconvoluted spectrum consists of three main components centered at 284 eV, 285.2 eV and 286.7 eV that correspond to sp^2 hybridized carbon, sp^3 carbon and C-O bonds, respectively[18]. It is well known that carbon dots are composed mainly of sp^3 hybridized carbon bonds, which in

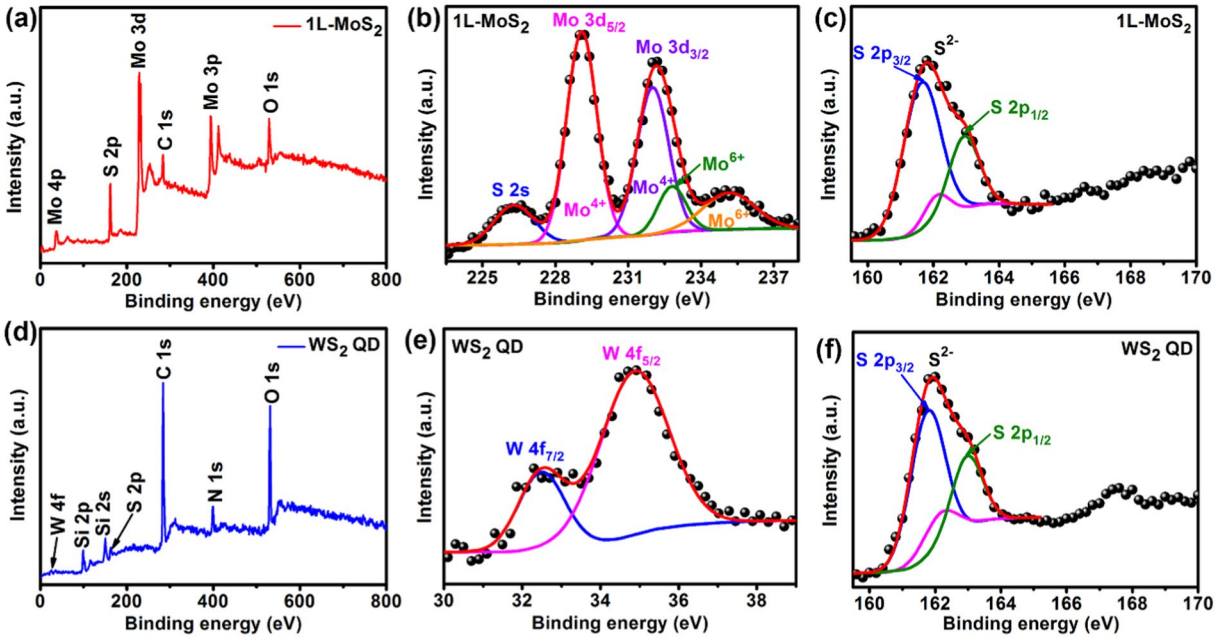

Figure 3. (**a**) XPS survey spectrum of 1L-MoS_2. (**b**,**c**) Core level XPS spectra of 1L-MoS_2 with fitting for Mo 3d, and S 2p, respectively. (**d**) XPS survey spectrum of WS_2 QD. (**e**,**f**) Core level XPS spectra of WS_2 QD with fitting for W 4 f and S 2p, respectively. The symbols are experimental data and the solid curves are Gaussian fittings.

our case, constitute merely of 5.8% of the high-resolution C 1 s spectrum. In contrast, the sp^2 hybridized carbon accounts for 73.9%. These results rule out the possible presence of any carbon dots in the WS_2 QDs samples. For the as-synthesized WS_2 QD, the peaks at 32.5 eV and 34.8 eV are identified to be from W $4f_{7/2}$ and W $4f_{5/2}$, respectively, corresponding to the 4 + oxidation state of W, as shown in Fig. 3(c), which are consistent with those reported for 2H-WS_2[21]. Figure 3(d) shows the S 2p XPS of the WS_2 QD with peaks at ~161.8 eV (S $2p_{3/2}$), and ~162.9 eV (S $2p_{1/2}$), which are similar to that of the 1L-MoS_2 sample. The existence of surface defects (S vacancies) in the WS_2 QD is shown by the presence of the peak at 162.1 eV (S $2p_{3/2}$) (with 13.5% spectral weight), which may be created during the synthesis by liquid exfoliation method. Additionally, there is a small peak at 167.5 eV corresponding to SO_2 which suggests the minor presence of oxidized sulfur edges.

Raman spectroscopy has been widely used for the determination of the number of layers[22], the strain, the external field and doping effects[16,23,24] in 2D TMDs. Figure 4(a) shows the comparative Raman spectra for 1L-MoS_2 and 1L-MoS_2/WS_2 QD HS at room temperature. Two characteristic Raman modes E_{2g} and A_{1g} corresponding to the in-plane vibration of Mo and S atoms and out-of-plane vibration of S atoms respectively can be clearly seen[22]. The frequency difference (Δk) between E_{2g} and A_{1g} modes has been used to identify the number of layers in MoS_2[22]. For 1L-MoS_2 sample, the measured Δk is ~19.6 cm^{-1} confirming the monolayer growth[22], which is consistent with the AFM result. WS_2 QDs also show the presence of two characteristic Raman modes E_{2g} and A_{1g} of WS_2, which confirms the crystallinity of the QDs[25]. A comparative Raman analysis of the WS_2 QDs and WS_2 nanosheets shows a red shift in the E_{2g} mode and a blue shift in the A_{1g} mode in the QDs with respect to that of the nanosheets (see Fig. S3, Supporting Information). This shift in the Raman modes is attributed to the decrease in the number of layers of the WS_2 QD compared to the WS_2 nanosheets[25]. Interestingly, after the formation of the 1L-MoS_2/WS_2 QD HS, the position of the Raman modes of MoS_2, A_{1g} is red-shifted by 1.2 cm^{-1}, while that of E_{2g} is not influenced (See Table 1). This shift occurs due to the fact that the A_{1g} mode couples much more strongly with electrons than the E_{2g} mode[23]. The redshift of the A_{1g} mode indicates an effective n-type doping effect in the MoS_2 layer due to the strong electron-phonon coupling[16]. Crystallinity of the WS_2 QDs is further confirmed from the XRD analysis (see Fig. S4, Supporting Information) that shows a strong peak at 14.3° corresponding to the (002) plane and multiple weak peaks corresponding to (004), (101), (103), (006) and (105) lattice planes of 2H-phase of crystalline WS_2 (JCPDS 08-0237)[26].

Figure 4(b) shows the UV-vis absorption spectra of the samples. The 1L-MoS_2 exhibits three excitonic absorption peaks A, B and C at 1.85, 2.00 and 2.74 eV, respectively. The excitonic A and B peaks originate from the transitions between the spin-orbit split valence band and the minimum of the conduction band at the K and K′ points of the Brillouin zone[7]. The C absorption peak is assigned to the direct transition from the deep valence band to the conduction band[27]. The absorption spectrum of WS_2 QDs (see Fig. 4(b)) shows low absorbance in the visible range and no distinct excitonic features in contrast to that of the monolayer WS_2 reported in the literature[28]. Since the QDs are mostly monolayer, the bandgap is expected to be direct type and the optical bandgap calculated from the Tauc plot is 3.45 eV (see Fig. S5, Supporting Information), which is much higher than that of the monolayer WS_2[28]. In case of 1L-MoS_2/WS_2 QD HS, three absorption peaks (A, B, C) were observed, which is consistent with the spectra of 1L-MoS_2. A marginal enhancement in the absorbance of 1L-MoS_2/WS_2 QD HS compared to that of individual absorbance of 1L-MoS_2 and WS_2 QDs is observed in the spectral range 2.48 to 4.59 eV. The

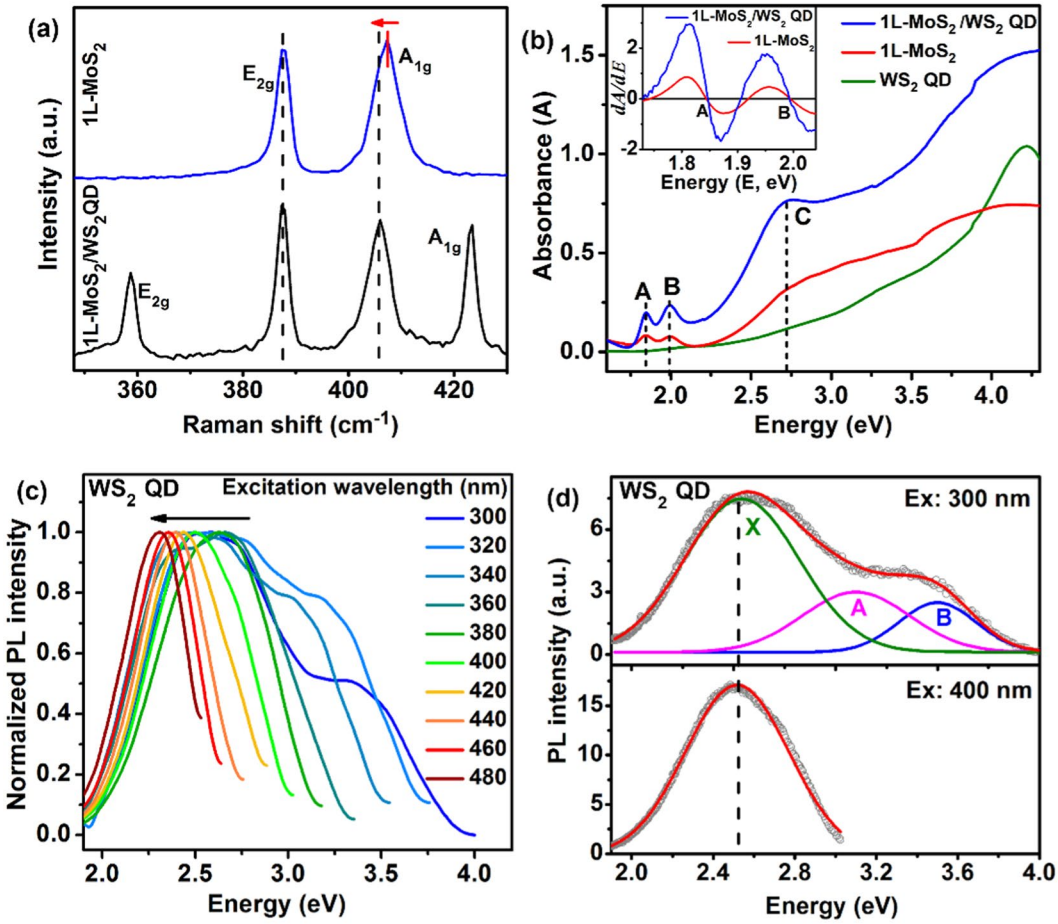

Figure 4. (**a**) Comparison of the Raman spectra of 1L-MoS_2 and 1L-MoS_2/WS_2 QD HS (with 24 mg/L concentration of WS_2 QD). The vertical dotted lines are indicative of no shift in the E_{2g} mode and a redshift of the A_{1g} Raman mode of MoS_2 in the 1L-MoS_2/WS_2 QD HS. (**b**) Comparison of the UV-visible absorption spectra of 1L-MoS_2, WS_2 QDs and 1L-MoS_2/WS_2 QD (with 24 mg/L concentration of WS_2 QD). A, B and C represent the characteristic excitonic absorption bands of the 1L-MoS_2. The inset shows the first derivative of the absorption spectra of 1L-MoS_2 and 1L-MoS_2/WS_2 QD to indicate any possible shift of A and B peaks. (**c**) Normalized PL emission spectra of WS_2 QDs for various excitation wavelengths (300–480 nm). (**d**) Gaussian fitting of the PL emission spectrum for the excitation of 300 nm and 400 nm. The constituent peaks are denoted as B, A, and X excitonic emissions.

Sample	Raman modes			Relative weightage of PL peaks			
	E_{2g} (cm^{-1})	A_{1g} (cm^{-1})	Δk (cm^{-1})	B-exciton (B) (%)	A-exciton (A) (%)	Trion (A^-) (%)	Bound exciton (X) (%)
1L-MoS_2	387.6	407.2	19.6	13.2	53.0	23.2	10.6
1L-MoS_2/WS_2 QD	387.6	406.0	18.4	15.5	20.6	37.2	26.7

Table 1. Summary of the Raman modes (E_{2g}, A_{1g}), their separation (Δk) and relative weightage of the PL peaks obtained through Gaussian deconvolution for 1L-MoS_2 and 1L-MoS_2/WS_2 QD HS.

enhancement of the absorbance of the 1L-MoS_2/WS_2 QD heterostructure compared to that of the pristine monolayer MoS_2 and WS_2 QDs may be due to the combined effect of the increase in the number of layers as well as the enhanced light-material interaction in the heterostructure[29]. To determine the absorption peaks of spin-orbit split B and A excitons in the 1L-MoS_2 and 1L-MoS_2/WS_2 QDs, we have taken the first derivative of the absorption spectra (see the inset of Fig. 4(b)). The A and B excitonic peaks for 1L-MoS_2 are located at 1.844 eV and 1.990 eV, respectively. For 1L-MoS_2/WS_2 QD HS, there is only ~4 meV redshift in the A excitonic peak with respect to the 1L-MoS_2. This small redshift in the A peak may be due to the n-type doping of 1L-MoS_2 after the formation of the HS due to the charge transfer from the WS_2 QDs to the 1L-MoS_2. In contrast to our case of charge transfer, the shift in the excitonic peaks in the absorption spectra has been more prominent in chemically doped 1L-MoS_2[30].

The as-synthesized WS_2 QDs are highly fluorescent in nature with a quantum yield (QY) of ~15%. The PL emission spectra usually depend on the wavelength of excitation due to the contribution from multiple states and size distribution[31]. Figure 4(c) displays the normalized PL emission spectra of the WS_2 QDs for various excitation wavelengths. As the excitation wavelength is increased systematically from 300 to 480 nm, the emission peak position systematically redshift from 2.52 eV to 2.31 eV. The excitation wavelength-dependent PL shift in WS_2 QDs is poorly understood in the literature. The broadening in PL peak usually results from the polydispersity in the WS_2 QD size, which is attributed to the colloidal synthesis process[32,33]. To explain the broad PL spectrum in WS_2 QDs under 300 nm excitation, we have deconvoluted the spectrum with three Gaussian peaks: the B exciton, the neutral A exciton, and the defect bound exciton X, as shown in Fig. 4(d). The A and B-excitons centered at 3.1 eV and 3.5 eV arise from the giant spin-orbit splitting of the valence band in the K-K′ point[21]. The B and A excitons arise from the splitting of the valence band at the K point due to strong spin-orbit coupling in the W atom of WS_2[7,34]. The energy difference between these two peaks is found to be ~400 meV, which is similar to that of monolayer WS_2[35]. The contribution from the A and B exciton is gradually reduced with increasing excitation wavelength and hence the spectrum is narrower than that with low wavelength excitation. The X band in the fitting at 2.54 eV is associated with the surface defect bound exciton X, and at higher excitation wavelength (>380 nm), the PL emission arises only from the bound exciton transition (Fig. 4(d)). Thus, the PL peak position is dictated by the excitation energy; lower the excitation energy lower will be the emission energy due to the selective excitation of energy levels. This explains the wavelength-dependent shift in the PL emission peaks in WS_2 QDs. Note that the PL peak assignments are based on the measured bandgap and the energy band relationship: $E_B = E_g - E_b + E_{SO}$[36], where E_b is the exciton binding energy (~0.3 eV for monolayer WS_2). E_{SO} is the energy difference arising due to splitting of the valence band due to strong spin-orbit coupling (~0.4 eV) in the W atom of WS_2[35]. Thus, based on the measured bandgap, E_B is expected to be ~3.5 eV. Likewise, the A exciton peak is expected at ~3.1 eV. The deconvoluted peaks positions in Fig. 4(d) closely match with the above. Note that the defect contribution to the PL intensity is very significant in all the spectra.

Figure 5(a) displays representative PL spectra of pristine 1L-MoS_2, WS_2 QD and 1L-MoS_2/WS_2 QD HS, measured with 488 nm laser excitation. The PL emission peak for the WS_2 QD is broad due to the size distribution of QDs and it is much weak compared that of the 1L-MoS_2. The PL peak position (~2.28 eV) is consistent with the result presented in Fig. 4(c)[37]. Interestingly, this peak is at a much higher energy than that of 1L-WS_2[28]. The broadening and blue shifting of the PL peak of the WS_2 QD originate from the quantum size effect as well as the surface defect states[31]. For 1L-MoS_2, we observe a PL peak at 1.86 eV with 488 nm excitation. However, after the formation of the 1L-MoS_2/WS_2 QD HS the PL peak position is redshifted by ~30 meV and the intensity is also partially quenched. Such a redshift and quenching of the PL is an indication of the charge transfer and n-doping effect due to the specific band alignment at the interface. This is consistent with the Raman analysis discussed earlier.

To further interpret the possible origin of the PL evolution, a deconvolution analysis was carried out by fitting each spectrum with four Gaussian peaks: the neutral exciton (A^0), negative trion (A^-), B exciton, and the defect bound exciton (X). Figure 5(b) shows the fitted PL spectra of the sample 1L-MoS_2 and 1L-MoS_2/WS_2 QD HS, respectively. The A^0 and B exciton peaks are associated with the direct bandgap transition at the K point in the Brillouin Zone, with energy split from the strong valence-band spin-orbit coupling[8]. It has been reported that the A^- trion peak arises from charged impurities in the 1L-MoS_2 grown by a CVD method on accounts of unintentional n-type doping[38], and the X exciton peak is assigned to the radiative recombination of bound excitons from the defect trap states[39]. Note that in the fitting process, we have fixed only the peak positions of the A^0 (1.88 eV), B (1.98 eV), A^- (1.83 eV) and the X (1.78 eV) bands and the rest are kept as free parameters. With the decoration of the WS_2 QDs, the PL spectral weight of the A^0 exciton peak decreased from 53% to 20.6%, while that of the A^- trion peak increased from 23.2% to 37.2% (see Fig. 4(b) and Table 1). This increase in the spectral weight of the negative trion in 1L-MoS_2/WS_2 QD HS is due to an increase in the number of excess electrons in the 1L-MoS_2. This is an indication that electrons are transferred from the WS_2 QDs to the 1L-MoS_2. Upon illumination (at 488 nm) with photon energy lesser than the bandgap (E_g) of the WS_2 QDs, only electrons in the defect states of the QDs absorb the photons and these electrons are excited to the conduction band. Some of these generated electrons are transferred to the 1L-MoS_2 resulting in n-type doping, as can be understood from the schematic of the band alignment of the 1L-MoS_2 and WS_2 QD depicted in Fig. 5(c). DFT calculations on the MoS_2/WS_2 HS from previous studies show charge transfer from 1L-WS_2 to 1L-MoS_2[40]. The spectral weight of the defect bound excitons X increases from 10.6% to 26.7% after the formation of HS. (see Fig. 4(b) and Table 1).

To provide evidence in support of the proposed charge transfer process, the change in the work function of 1L-MoS_2 before and after the decoration of WS_2 QD was estimated by KPFM (Kelvin probe force microscopy). Figure 6(a,c) show the AFM topography of 1L-MoS_2 and 1L-MoS_2/WS_2 QD HS, while Fig. 6(b,d) show the surface potential image of 1L-MoS_2 and 1L-MoS_2/WS_2 QD HS, respectively. Before measurement, the work function of the tip (Φ_t, in eV) was calibrated (~4.52 eV). The overall contact potential difference (V_{CPD}, in V) values of the measured samples were provided by the KPFM measurements. The measured V_{CPD} between the sample and the tip can be expressed as, $e \times V_{CPD} = \Phi_t - \Phi_s$, where e is the elementary charge and Φ_s is the work function of the sample. The contact potential difference for 1L-MoS_2 is ~85 mV, while that for 1L-MoS_2/WS_2 QD HS is ~120 mV. So, the work functions of 1L- MoS_2, $\Phi_{1L\text{-}MoS2}$ ~ 4.435 eV, which is similar to previously reported values[41] and $\Phi_{1L\text{-}MoS2/WS2}$ ~ 4.400 eV, respectively. Thus, there is a distinct decrease in the work function of the 1L-MoS_2/WS_2 QD HS by 35 meV compared to 1L-MoS_2. The reduction in the work function of the HS suggests the favorable band bending for the charge transfer from the WS_2 QDs to the 1L-MoS_2.

To further understand the change of the PL intensity of the 1L-MoS_2 with the addition of the WS_2 QDs (concentration 4 to 36 mg/L), PL intensity was measured for the HS system. Figure 7(a) shows the variation of the PL spectra of the 1L-MoS_2 with different concentrations of WS_2 QDs. The PL intensity of the 1L-MoS_2 decreases systematically and PL peak broadens and red-shifts as the concentration of the WS_2 QDs is increased. The total PL

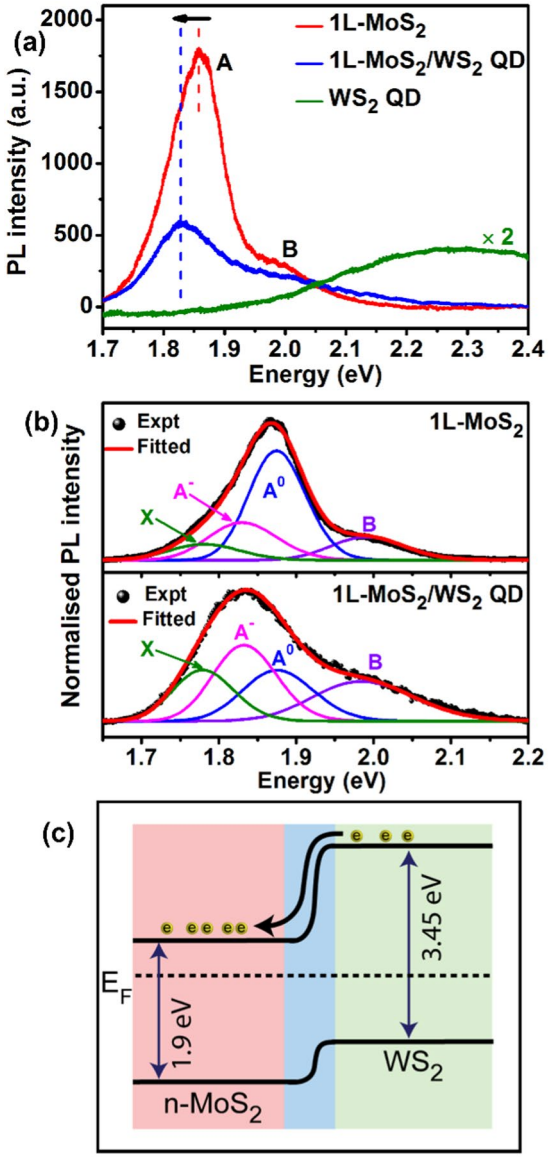

Figure 5. (**a**) Comparative PL spectra of pristine 1L-MoS_2, WS_2 QDs and 1L-MoS_2/WS_2 QD HS (with 24 mg/L concentration of WS_2 QD) measured with 488 nm excitation using a micro-Raman system. (**b**) Gaussian deconvolution of PL spectra of pristine 1L-MoS_2 and 1L-MoS_2/WS_2 QD HS, respectively. (**c**) Energy band diagram of the 1L-MoS_2/WS_2 QD heterostructure under equilibrium.

intensity of the 1L-MoS_2 decreases dramatically after the formation of the 1L-MoS_2/WS_2 QD HS even at very low concentration (4 mg/L), as shown in Fig. 7(b). Note that attachment of WS_2 QDs to 1L-MoS_2 surface is limited by the specific surface area of the 1L-MoS_2 and beyond a certain concentration, WS_2 QDs are not directly attached to the MoS_2 surface sites and hence further charge transfer is restricted at high concentration. To have a better understanding of the spectral changes in PL, we have considered the contribution of the neutral exciton, trion and defect bound exciton in the spectral deconvolution of PL peaks, as shown in Fig. 7(c). We believe that with increasing concentration of WS_2 QDs, charge carrier density increases in 1L-MoS_2. These doped electrons easily form trions and restrain the electron-hole pair recombination and as a result, the PL intensity quenches systematically and the PL peak is redshifted. Therefore, the neutral excitons are gradually converted to trions resulting in the change of the spectral weight of the individual component. It is evident from the fitting shown in Fig. 7(c), for low concentrations of the WS_2 QD (<12 mg/L), the PL emission is dominated by the neutral exciton peak (A^0). At higher concentration of WS_2 QDs, the contribution of the trions becomes higher than the neutral exciton and hence induces quenching of the PL intensity and a redshift of the PL peak position. Figure 8(a) shows a plot of the integrated PL intensity of neutral excitons I_{A^0}, negative trions I_{A^-} and the bound excitons I_X as a function of the concentration of WS_2 QDs. We notice that the intensity of the neutral excitons I_{A^0} decreases gradually and then almost saturates at high concentration of the WS_2 QD (>24 mg/L). However, there is a very small change in the integrated intensity of the trions. This is because the trion emission saturates after a certain doping level due to Pauli blocking effect[15]. Thus, the excess electrons that are transferred from the WS_2 QDs to the 1L-MoS_2 will

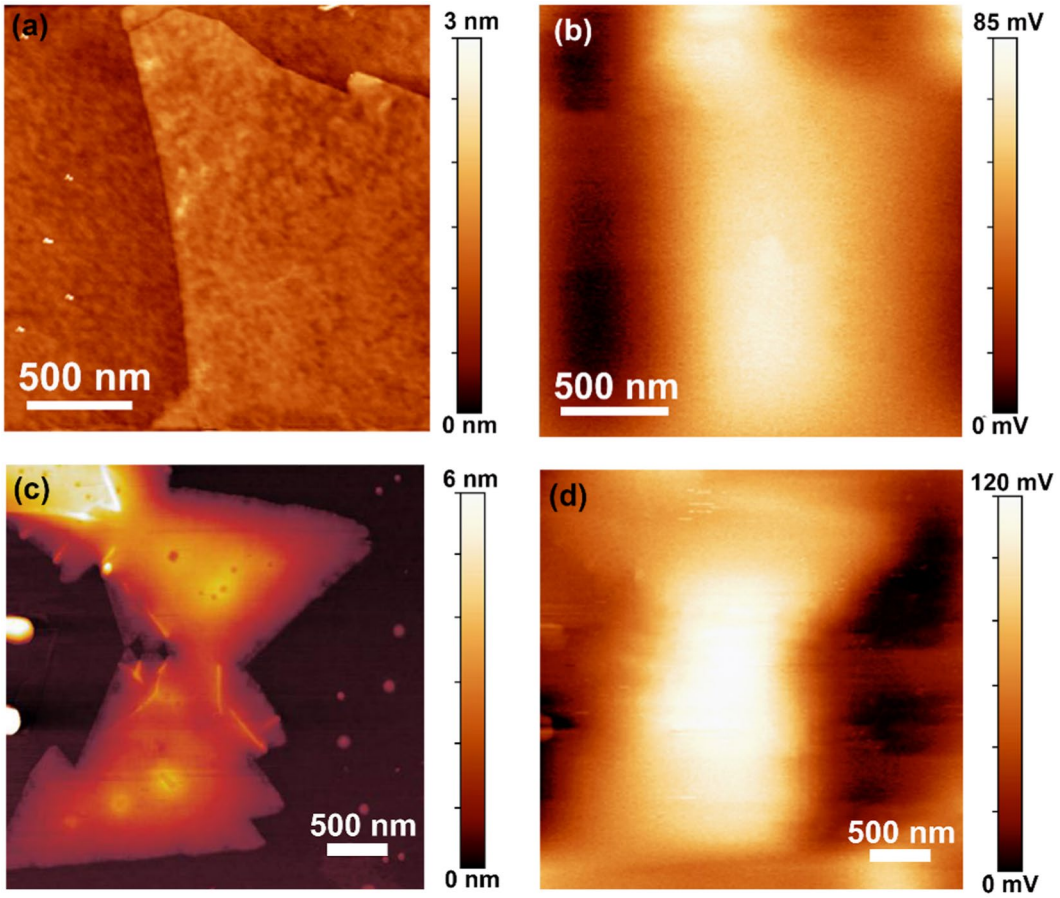

Figure 6. (**a**,**c**) AFM surface topography images of 1L-MoS_2 and 1L-MoS_2/WS_2 QD, respectively. (**b**,**d**) The corresponding KPFM surface potential images.

further move to the defect trap states. It is interesting to note that despite the systematic decrease in the integrated PL intensity of A^0 and A^- peaks, the defect-related X peak intensity does not decrease with doping, which is essentially due to the charge transfer from the A^- level to X level. In the absence of defect, one would expect an increase in trion population with increasing doping (electron) concentration, which is contrary to our experimental data. On the other hand, the total integrated PL intensity I_{Total} decreases in a similar way as that of I_{A^0}. Figure 8(b) shows the change of the PL spectral weight of the neutral exciton (I_{A^0}/I_{Total}) with the increase in the concentration of the WS_2 QDs. For pristine 1L-MoS_2 the spectral weight is ~0.61, whereas, with doping at higher concentration (>24 mg/L), the spectral weight decreases up to ~0.29. This is an indication of the transition from neutral exciton to trion with the increase in the doping.

For a quantitative understanding of the relative change in the PL intensity of the neutral exciton I_{A^0}, trion I_{A^-} and defect bound exciton I_X, we discuss the exciton and trion relaxation dynamics with rate equations based on a four-energy level model, as shown in Fig. 8(c) [42]. Here, G represents the generation rate of excitons, Γ_1 and Γ_2 represent the decay rates of the exciton and trions, respectively. $k_{tr}(\delta)$ is the formation rate of trion from the exciton, which is dependent on the doping concentration (δ) of the WS_2 QDs. To better model our experimental observation, we have assumed Γ_1 to be dependent of δ and it is taken as proportional to doping concentration δ, without which the trion population would not decay with increasing δ, which will be evident from the solution of the rate equations discussed below. In case of high doping density, carrier-density-dependent recombination dynamics of excitons is rational and it has been reported for InGaN/GaN quantum wells[43]. Thus the dependence of Γ_1 on δ is reasonable in the present case. The trions also decay through the defect trapping state at the rate Γ_3. Lastly, Γ_4 represents the decay rate of the defect bound excitons. Thus, based on the evolution of the three peaks with different doping concentrations, the electronic transitions are shown in Fig. 8(c). The corresponding rate equations for the population of neutral excitons N_{A^0}, trions N_{A^-} and the defect bound excitons N_X can be expressed as:

$$\frac{dN_{A^0}}{dt} = G - [\Gamma_1(\delta) + k_{tr}(\delta)]N_{A^0} \quad (1)$$

$$\frac{dN_{A^-}}{dt} = k_{tr}(\delta)N_{A^0} - (\Gamma_2 + \Gamma_3)N_{A^-} \quad (2)$$

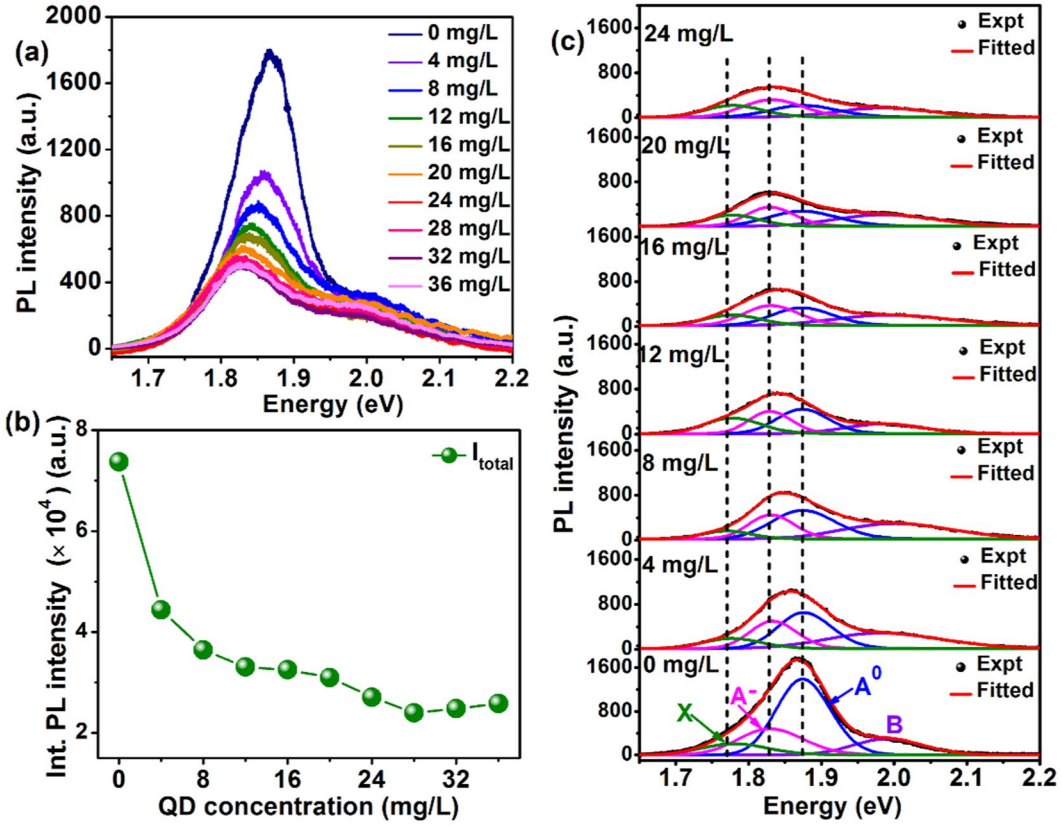

Figure 7. (**a**) Evolution of the PL spectra of the 1L-MoS_2 in presence of different concentrations of WS_2 QDs. (**b**) Integrated PL intensity of 1L-MoS_2 as a function of the concentration of WS_2 QDs. (**c**) Gaussian deconvolution of the PL spectra of 1L-MoS_2 measured at different concentration of the WS_2 QD. The PL spectra are deconvoluted with four peaks: B exciton (B), neutral exciton (A^0), trion (A^-), and the defect bound exciton (X).

$$\frac{dN_X}{dt} = \Gamma_3 N_{A^-} - \Gamma_4 N_X \tag{3}$$

$$k_{tr}(\delta) = k_{tr}(0)\left(1 - s.\frac{1}{\alpha\delta + 1}\right) \tag{4}$$

$$\Gamma_1(\delta) = \Gamma_1(0)(1 + \beta\delta) \tag{5}$$

where the parameter α in Eq. (4) represents the WS_2 QD adsorption probability and β in Eq. (5) is a proportionality constant. Considering that the rate of adsorption of WS_2 QDs obeys the Langmuir's law, the formation rate of trions with doping concentrations can be described as $k_{tr}(\delta)$ and s (~85% for our best-fitted data) reflects the ability of charge transfer from WS_2 QD to 1L-MoS_2. Doping concentration δ is increased in steps for 4 mg/L in our experiment. By solving the above rate equations analytically within the framework of the four-level model (see Section S1, Supporting Information, for the full derivation), under steady-state condition, the equations reduce to

$$N_{A^0}(\delta) = \frac{G}{\Gamma_1(\delta) + k_{tr}(\delta)} \tag{6}$$

$$N_{A^-}(\delta) = \frac{k_{tr}(\delta)}{(\Gamma_2 + \Gamma_3)}\frac{G}{(\Gamma_1(\delta) + k_{tr}(\delta))} \tag{7}$$

$$N_X(\delta) = \frac{\Gamma_3}{\Gamma_4}\frac{k_{tr}(\delta)}{(\Gamma_2 + \Gamma_3)}\frac{G}{(\Gamma_1(\delta) + k_{tr}(\delta))} \tag{8}$$

The steady-state PL intensities of neutral exciton (I_{A^0}), trion (I_{A^-}) and defect bound exciton (I_X) can be represented as follows:

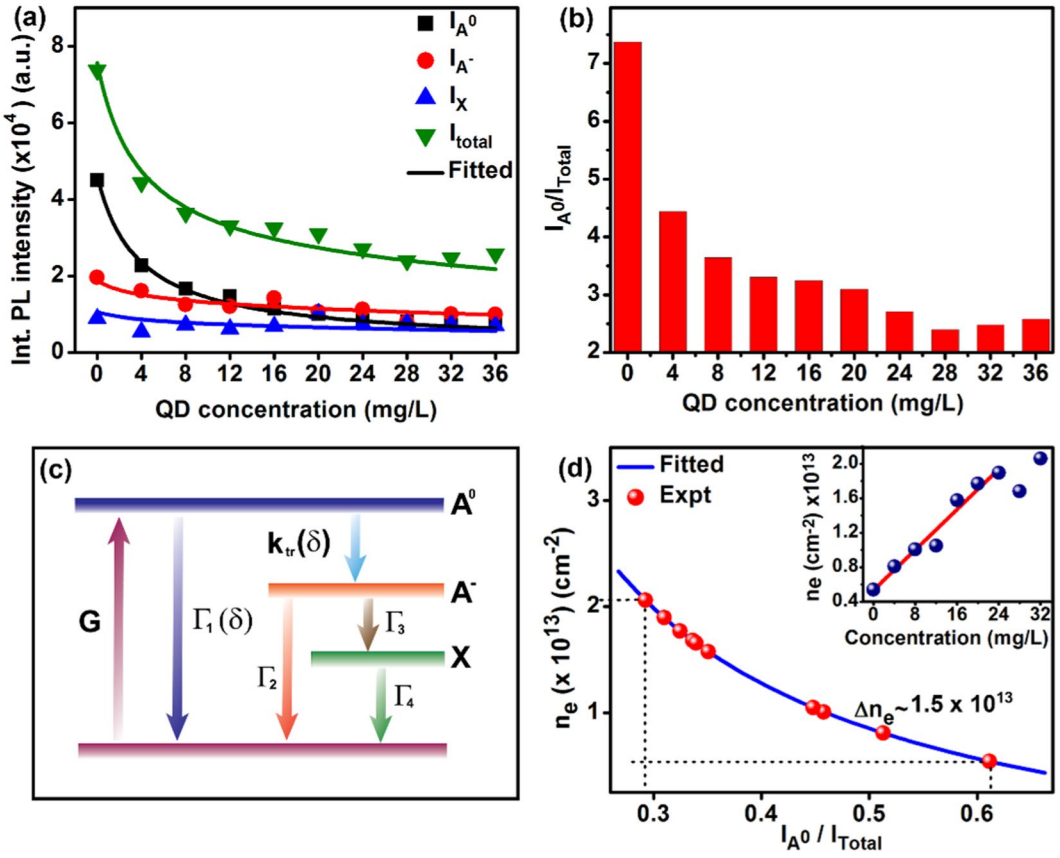

Figure 8. (**a**) Integrated PL intensity of neutral exciton (I_{A^0}), trion (I_{A^-}), defect bound exciton (I_X) and the sum (I_{Total}) of I_{A^0}, I_{A^-} and I_X as a function of the concentration of WS_2 QD. Symbols are the experimental data, while the solid lines are fitted data based on analytical solutions of rate equations. (**b**) The neutral exciton spectral weight (I_{A^0}/I_{Total}) as a function of the concentration of WS_2 QD. (**c**) Schematic representation of electronic transitions through a four-level energy diagram involving the neutral exciton (I_{A^0}), trion (I_{A^-}), defect bound exciton (I_X) and the ground state. Other symbols are described in the text. (**d**) Calculation of electron density (n_e) based on the law of mass action; inset shows n_e as a function of the concentration of WS_2 QDs.

$$I_{A^0}(\delta) = \frac{AG\gamma_{ex}}{\Gamma_1(\delta) + k_{tr}(\delta)} \tag{9}$$

$$I_{A^-}(\delta) = \frac{k_{tr}(\delta)}{(\Gamma_2 + \Gamma_3)} \frac{AG\gamma_{tr}}{(\Gamma_1(\delta) + k_{tr}(\delta))} \tag{10}$$

$$I_X(\delta) = \frac{\Gamma_3}{\Gamma_4} \frac{k_{tr}(\delta)}{(\Gamma_2 + \Gamma_3)} \frac{AG\gamma_X}{(\Gamma_1(\delta) + k_{tr}(\delta))} \tag{11}$$

where A is the collection efficiency of luminescence, γ_{ex}, γ_{tr} and γ_X are the radiative decay rates of neutral exciton, trion and defect bound exciton, respectively. The calculated/fitted PL intensities I_{A^0}, I_{A^-} and I_X in Eqs. (9–11), are in excellent agreement with the experimental results, as shown in Fig. 8(a). The parameters used in this analysis are $\Gamma_1(0) = 0.002\,ps^{-1}$, $\Gamma_2 = 0.02\,ps^{-1}$, $\Gamma_3 = 0.05\,ps^{-1}$, and $k_{tr}(0) = 0.5\,ps^{-1}$, which are based on previously reported data[42,44]. We have assumed an intermediate decay rate from the defect trap state, $\Gamma_4 = 0.01\,ps^{-1}$ for a good fit to the carrier recombination dynamics. The fitting parameters of $AG\gamma_{tr}/AG\gamma_{ex}$ and $AG\gamma_X/AG\gamma_{ex}$ to match the experimental data are 0.38 and 0.01, respectively, which implies that $\gamma_{tr} < \gamma_{ex}$ and $\gamma_X \ll \gamma_{ex}$, consistent with their relative PL intensities observed experimentally. Note that our value of γ_{tr}/γ_{ex} is nearly double of the reported value ($\gamma_{tr}/\gamma_{ex} = 0.15$)[12], due to the specific band alignment for favorable charge transfer and formation of trions. Due to the higher bandgap of WS_2 QDs than that of monolayer WS_2, the band bending is higher in our case resulting in more efficient charge transfer. Our results further imply that the defect (X) contribution to the PL evolution is smaller than the trion (A^-) contribution. However, it is significant enough and necessary to consider it in the rate equation to match with the experimental data.

Assuming the validity of the law of mass action here, the relationship between the population of the neutral exciton (N_{A^0}), trions (N_{A^-}) and the charge density n_e in the 1L-MoS_2 is expressed as

$$\frac{N_{A^0} n_e}{N_{A^-}} = \left(\frac{16\pi m_{A^0} m_e}{h^2 m_{A^-}}\right) k_B T \exp\left(-\frac{E_b}{k_B T}\right) \tag{12}$$

where h is the Planck's constant, k_B is the Boltzmann constant, T is the temperature and E_b is the trion binding energy. The effective masses of the electron, hole, and trion are m_e, m_h and m_{A^-}, respectively. m_e and m_h are 0.35 m_0 and 0.45 m_0, where m_0 is a free electron mass[15]. Therefore, the effective mass of a neutral exciton (m_{A^0}) and a trion (m_{A^-}) can be calculated as $m_{A^0} = m_e + m_h = 0.8\ m_0$, $m_{A^-} = 2m_e + m_h = 1.15\ m_0$, respectively. Therefore, the calculated the PL spectral weight of the exciton can be expressed as

$$\frac{I_{A^0}}{I_{total}} = \frac{1}{1 + \frac{\gamma_{tr} N_{A^-}}{\gamma_{ex} N_{A^0}} + \frac{\gamma_X N_X}{\gamma_{ex} N_{A^0}}} \approx \frac{1}{1 + 7.4 \times 10^{-14} n_e + 4.4 \times 10^{-14} n_e} \approx \frac{1}{1 + 11.8 \times 10^{-14} n_e} \tag{13}$$

where $I_{total} = I_{A^0} + I_{A^-} + I_X$, and the E_b and T are taken as 25 meV and 300 K, respectively. The γ_{tr}/γ_{ex} and γ_X/γ_{ex} values as obtained from the fitting are substituted here. Thus, the charge density n_e is calculated from the exciton spectral weight using Eq. (13) and is shown in Fig. 8(d). For pristine 1L-MoS_2, the charge density is ~ $5.5 \times 10^{12}\ cm^{-2}$ owing to its unintentional n-doping attributes[45]. After WS_2 QD doping, in the saturation region, the calculated electron density of the 1L-MoS_2/WS_2 QD HS increases to $20.5 \times 10^{12}\ cm^{-2}$. It is important to note that the difference in the electron density before and after the formation of the HS is, $\Delta n_e \sim 1.5 \times 10^{13}\ cm^{-2}$, which is significant. This change in the electron density signifies the approximate density of doped electrons in 1L-MoS_2. The inset in Fig. 8(d) shows the gradual increase in the charge density n_e in the 1L-MoS_2 with the increase in the WS_2 QD concentration. Thus, these results demonstrate effective control of doping/electron density in 1L-MoS_2 about one order of magnitude by the decoration of WS_2 QDs. We believe that the electron density in the 2D materials can be effectively tuned by decorating with QDs of other 2D materials with high bandgap and thus, enable suitable control of the electrical and optical properties of the 2D materials, which is very significant for the ensuing applications.

Conclusion

In conclusion, we have demonstrated the tunability in the light emission of the 1L-MoS_2 by decorating it with the WS_2 QD. KPFM analysis revealed a decrease in the work function of 1L-MoS_2 with the decoration of WS_2 QDs. Systematic quenching of the PL intensity of 1L-MoS_2 with the decoration of WS_2 QDs was explained on the basis of charge transfer from WS_2 QDs to 1L-MoS_2. A detailed analysis using coupled charge transfer among four-energy levels was employed to explain the redshift and the decrease in the PL intensity of the 1L-MoS_2 after decoration with the WS_2 QDs. An analytical solution to the coupled rate equations for change in the population of different excitonic emissions including bound excitonic transition was successfully employed to quantitatively understand the quenching process. The contribution of defects in the charge transfer induced quenching of PL and the carrier-density-dependent recombination dynamics of excitons were established through the quantitative analysis of the spectral evolution. Charge transfer induced increase in electron density in 1L-MoS_2 leads to the transition of the neutral excitons to trions. The change in the electron density up to $\Delta n_e \sim 1.5 \times 10^{13}\ cm^{-2}$ indicates high n-type doping in the 1L-MoS_2 by a simple decoration approach. Our results suggest an effective way to manipulate the electron density through decoration/doping technique, which is advantageous to tune the optical and electrical properties of monolayer TMDs for optoelectronic applications.

Methods

Synthesis of WS_2 quantum dots. High purity WS_2 powder (Sigma Aldrich, 99%) was dispersed in 80 ml N-methyl-2-pyrrolidinone (NMP) (Alfa Aesar, HPLC grade, 95%) and tip-sonicated using an ultrasonic homogenizer (Sonic Ruptor 250, Omni International) for 15 hours. Subsequently, the suspension was allowed to settle for 12 hours and was centrifuged for 45 minutes at 12000 rpm. The top 2/3rd of the solution (supernatant) contains the WS_2 quantum dots, while the bottom 1/3rd (centrifugate) comprises of the bigger WS_2 quantum dots and the nanosheets (See Fig. S6, Supporting Information). The excess solvent from the centrifugate was evaporated with constant stirring and the resultant residue was dispersed in Milli-Q water at various concentrations (4, 8, 12, 16, 20, 24, 28, 32, 36 mg/L) for further experiments.

Growth of monolayer MoS_2 by chemical vapor deposition (CVD) technique and formation of heterostructure with WS_2 quantum dots. Monolayer MoS_2 film was synthesized on Si/SiO_2 and Sapphire substrates by the CVD method using a two-zone horizontal muffle furnace. 15 mg of MoO_3 powder (99.5%, Sigma-Aldrich) and 200 mg of sulfur powder (99.95%, Sigma-Aldrich) in separate quartz boats were placed inside the 2" diameter quartz tube at the center of their respective zones for the CVD growth of MoS_2, as reported previously[46]. The substrates were placed face down on top of the quartz mask with a circular opening and then placed on the boat containing MoO_3. Then, the quartz tube was flushed with high purity argon gas at 300 sccm for 30 minutes prior to the growth. The sources temperatures were gradually increased from room temperature to 700 °C and 150 °C at the rates 15 and 3.5 °C/min for MoO_3 and Sulphur, respectively, and kept at this temperature for 5 minutes at an argon flow rate of 10 sccm. Afterward, the furnace is allowed to cool down to room temperature. It was observed that the 1L-MoS_2 film was deposited only on the portions of the substrate which were covered by the quartz mask. The unmasked regions of the substrate were found to be deposited with few-layer and multilayer MoS_2. We observed that in both the SiO_2/Si and sapphire substrates, large-area monolayer MoS_2 film was grown as reported in our previous work[47].

For the formation of the heterostructure, WS_2 QDs were spin-coated onto the 1L-MoS_2 and are dried before optical characterizations were carried out (see Fig. S6, Supporting Information).

Characterization techniques. The 1L-MoS_2 grown over various substrates, WS_2 QDs, and their heterostructure were studied by high-resolution micro-Raman spectroscopy (LabRam HR800, Jobin Yvon). Both Raman and PL spectra were acquired sequentially from the same spot on the sample through a 100X objective lens with a spot size ~1 μm and laser power ~1.5 mW to avoid laser-induced sample damage. The signal was then collected by a charge-coupled device (CCD) using a backscattering geometry sent through a multimode fiber grating (1800 grooves mm^{-1}). Atomic force microscopy (AFM) (Cypher, Oxford Instruments) images were acquired to confirm the layer thickness of CVD-grown MoS_2 and WS_2 quantum dots. In order to carry out the surface potential (SP) analysis of the samples, the Kelvin probe force microscopy (KPFM) measurements were done. Conducting platinum (Pt)/iridium (Ir)-coated tips were used for KPFM studies, having the optimum frequency of operation ~72 kHz. To avoid the noise between the topographical and the surface potential measuring images, the measurements were carried out in the dual-pass lift mode. The calculation of the work function for the sample (Φ_s) was obtained from the AFM by using Pt/Ir tips in the KPFM mode. The morphology, size and structural properties of the as-prepared WS_2 QDs were studied by a transmission electron microscope (TEM) (JEOL-JEM 2010 operated at 200 kV). Samples for TEM analysis were prepared on a carbon-coated Cu grid of 400 mesh size (Pacific Grid, USA). TEM imaging was used to examine the decoration of WS_2 QD on 1L-MoS_2. For this purpose, the CVD grown 1L-MoS_2 was transferred from the SiO_2 substrates to carbon-coated Cu-grids. To transfer as-grown MoS_2 film, the sample was coated with polymethylmethacrylate (PMMA) by spin coating at 1500 rpm for 60 s, and then baked at 140 °C for 10 min. The PMMA-coated sample was then treated with 6 M NaOH solution for one hour to etch out the PMMA supported MoS_2 film, which was then repeatedly washed with DI water. Then, the film was fished out onto a Cu grid and allowed to dry at low temperature (50 °C). The PMMA was removed from the MoS_2 film by the addition of acetone dropwise. WS_2 QDs of the concentration 4 mg/L was then drop cast on the sample for TEM imaging. A commercial spectrophotometer (PerkinElmer, Lambda 950) was used to study the UV−vis absorption spectra of the 1L-MoS_2/WS_2 QD HS as well as its individual counterparts.

Received: 4 June 2019; Accepted: 5 November 2019;
Published online: 19 December 2019

References

1. Radisavljevic, B., Radenovic, A., Brivio, J., Giacometti, V. & Kis, A. Single-layer MoS_2 transistors. *Nat. Nanotechnol.* **6**, 147, https://doi.org/10.1038/nnano.2010.279 (2011).
2. Lee, H. S. *et al.* MoS_2 Nanosheet Phototransistors with Thickness-Modulated Optical Energy Gap. *Nano Lett.* **12**, 3695–3700, https://doi.org/10.1021/nl301485q (2012).
3. Yu, X. *et al.* A high performance, visible to mid-infrared photodetector based on graphene nanoribbons passivated with HfO_2. *Nanoscale* **8**, 327–332, https://doi.org/10.1039/C5NR06869J (2016).
4. Paul, K. K., Mawlong, L. P. L. & Giri, P. K. Trion-Inhibited Strong Excitonic Emission and Broadband Giant Photoresponsivity from Chemical Vapor-Deposited Monolayer MoS_2 Grown *in Situ* on TiO_2 Nanostructure. *ACS Applied Materials & Interfaces* **10**, 42812–42825, https://doi.org/10.1021/acsami.8b14092 (2018).
5. Ghorai, A., Bayan, S., Gogurla, N., Midya, A. & Ray, S. K. Highly Luminescent WS_2 Quantum Dots/ZnO Heterojunctions for Light Emitting Devices. *ACS Applied Materials & Interfaces* **9**, 558–565, https://doi.org/10.1021/acsami.6b12859 (2017).
6. Koo, W.-T. *et al.* Few-Layered WS_2 Nanoplates Confined in Co, N-Doped Hollow Carbon Nanocages: Abundant WS_2 Edges for Highly Sensitive Gas Sensors. *Advanced Functional Materials* **28**, 1802575, https://doi.org/10.1002/adfm.201802575 (2018).
7. Mak, K. F., Lee, C., Hone, J., Shan, J. & Heinz, T. F. Atomically Thin MoS_2: A New Direct-Gap Semiconductor. *Phys. Rev. Lett.* **105**, 136805 (2010).
8. Splendiani, A. *et al.* Emerging Photoluminescence in Monolayer MoS_2. *Nano Lett.* **10**, 1271–1275, https://doi.org/10.1021/nl903868w (2010).
9. Li, H., Wu, J., Yin, Z. & Zhang, H. Preparation and Applications of Mechanically Exfoliated Single-Layer and Multilayer MoS_2 and WSe_2 Nanosheets. *Accounts of Chemical Research* **47**, 1067–1075, https://doi.org/10.1021/ar4002312 (2014).
10. Lopez-Sanchez, O., Lembke, D., Kayci, M., Radenovic, A. & Kis, A. Ultrasensitive photodetectors based on monolayer MoS_2. *Nature Nanotechnology* **8**, 497, https://doi.org/10.1038/nnano.2013.100 (2013).
11. Tao, Y. *et al.* Bright monolayer tungsten disulfide via exciton and trion chemical modulations. *Nanoscale* **10**, 6294–6299, https://doi.org/10.1039/C7NR09442F (2018).
12. Mouri, S., Miyauchi, Y. & Matsuda, K. Tunable Photoluminescence of Monolayer MoS_2 via Chemical Doping. *Nano Lett.* **13**, 5944–5948, https://doi.org/10.1021/nl403036h (2013).
13. Kang, Y. *et al.* Plasmonic Hot Electron Induced Structural Phase Transition in a MoS_2 Monolayer. *Advanced Materials* **26**, 6467–6471, https://doi.org/10.1002/adma.201401802 (2014).
14. Ross, J. S. *et al.* Electrical control of neutral and charged excitons in a monolayer semiconductor. *Nature Communications* **4**, 1474, https://doi.org/10.1038/ncomms2498 (2013).
15. Mak, K. F. *et al.* Tightly bound trions in monolayer MoS_2. *Nature Materials* **12**, 207, https://doi.org/10.1038/nmat3505 (2012).
16. Li, Z. *et al.* Graphene Quantum Dots Doping of MoS_2 Monolayers. *Advanced Materials* **27**, 5235–5240, https://doi.org/10.1002/adma.201501888 (2015).
17. Roy, S. *et al.* Observation of Charge Transfer in Heterostructures Composed of $MoSe_2$ Quantum Dots and a Monolayer of MoS_2 or WSe_2. *The Journal of Physical Chemistry C* **121**, 1997–2004, https://doi.org/10.1021/acs.jpcc.6b11778 (2017).
18. Mawlong, L. P. L., Paul, K. K. & Giri, P. K. Direct Chemical Vapor Deposition Growth of Monolayer MoS_2 on TiO_2 Nanorods and Evidence for Doping-Induced Strong Photoluminescence Enhancement. *The Journal of Physical Chemistry C* **122**, 15017–15025, https://doi.org/10.1021/acs.jpcc.8b03957 (2018).
19. Qi, J., Liu, H., Luo, Y., Zhang, D. & Wang, Y. Influences of added sand-dust particles on the tribological performance of graphite-like coating under solid–liquid lubrication. *Tribology International* **71**, 69–81, https://doi.org/10.1016/j.triboint.2013.11.003 (2014).
20. Baker, M. A., Gilmore, R., Lenardi, C. & Gissler, W. XPS investigation of preferential sputtering of S from MoS_2 and determination of MoS_x stoichiometry from Mo and S peak positions. *Applied Surface Science* **150**, 255–262, https://doi.org/10.1016/S0169-4332(99)00253-6 (1999).

21. Kondekar, N. P., Boebinger, M. G., Woods, E. V. & McDowell, M. T. *In Situ* XPS Investigation of Transformations at Crystallographically Oriented MoS_2 Interfaces. *ACS Applied Materials & Interfaces* **9**, 32394–32404, https://doi.org/10.1021/acsami.7b10230 (2017).
22. Lin, L. *et al*. Fabrication of Luminescent Monolayered Tungsten Dichalcogenides Quantum Dots with Giant Spin-Valley Coupling. *ACS Nano* **7**, 8214–8223, https://doi.org/10.1021/nn403682r (2013).
23. Li, H. *et al*. From Bulk to Monolayer MoS_2: Evolution of Raman Scattering. *Adv. Funct. Mater.* **22**, 1385–1390, https://doi.org/10.1002/adfm.201102111 (2012).
24. Chakraborty, B. *et al*. Symmetry-dependent phonon renormalization in monolayer MoS_2 transistor. *Physical Review B* **85**, 161403, https://doi.org/10.1103/PhysRevB.85.161403 (2012).
25. Tongay, S. *et al*. Broad-Range Modulation of Light Emission in Two-Dimensional Semiconductors by Molecular Physisorption Gating. *Nano Letters* **13**, 2831–2836, https://doi.org/10.1021/nl4011172 (2013).
26. Berkdemir, A. *et al*. Identification of individual and few layers of WS_2 using Raman Spectroscopy. *Scientific Reports* **3**, 1755, https://doi.org/10.1038/srep01755 (2013).
27. Yin, W. *et al*. Rational Control of Size and Photoluminescence of WS_2 Quantum Dots for White Light-Emitting Diodes. *ACS Applied Materials & Interfaces* **10**, 43824–43830, https://doi.org/10.1021/acsami.8b17966 (2018).
28. Wilcoxon, J. P. & Samara, G. A. Strong quantum-size effects in a layered semiconductor: ${\mathrm{MoS}}_{2}$ nanoclusters. *Physical Review B* **51**, 7299–7302, https://doi.org/10.1103/PhysRevB.51.7299 (1995).
29. Gutiérrez, H. R. *et al*. Extraordinary Room-Temperature Photoluminescence in Triangular WS_2 Monolayers. *Nano Letters* **13**, 3447–3454, https://doi.org/10.1021/nl3026357 (2013).
30. Wang, W. *et al*. Investigation of the band alignment at $MoS_2/PtSe_2$ heterojunctions. *Applied Physics Letters* **114**, 201601, https://doi.org/10.1063/1.5097248 (2019).
31. Dhakal, K. P. *et al*. Confocal absorption spectral imaging of MoS_2: optical transitions depending on the atomic thickness of intrinsic and chemically doped MoS_2. *Nanoscale* **6**, 13028–13035, https://doi.org/10.1039/C4NR03703K (2014).
32. Xu, S., Li, D. & Wu, P. One-Pot, Facile, and Versatile Synthesis of Monolayer MoS_2/WS_2 Quantum Dots as Bioimaging Probes and Efficient Electrocatalysts for Hydrogen Evolution Reaction. *Advanced Functional Materials* **25**, 1127–1136, https://doi.org/10.1002/adfm.201403863 (2015).
33. Lin, H. *et al*. Colloidal synthesis of MoS_2 quantum dots: size-dependent tunable photoluminescence and bioimaging. *New Journal of Chemistry* **39**, 8492–8497, https://doi.org/10.1039/C5NJ01698C (2015).
34. Wang, N. *et al*. Synthesis of Strongly Fluorescent Molybdenum Disulfide Nanosheets for Cell-Targeted Labeling. *ACS Applied Materials & Interfaces* **6**, 19888–19894, https://doi.org/10.1021/am505305g (2014).
35. Molas, M. R., Nogajewski, K., Potemski, M. & Babiński, A. Raman scattering excitation spectroscopy of monolayer WS_2. *Scientific Reports* **7**, 5036, https://doi.org/10.1038/s41598-017-05367-0 (2017).
36. Chernikov, A. *et al*. Exciton Binding Energy and Nonhydrogenic Rydberg Series in Monolayer WS_2. *Physical Review Letters* **113**, 076802, https://doi.org/10.1103/PhysRevLett.113.076802 (2014).
37. Li, Z.-W., Hu, Y.-H., Li, Y. & Fang, Z.-Y. Light–matter interaction of 2D materials: Physics and device applications. *Chinese Physics B* **26**, 036802, https://doi.org/10.1088/1674-1056/26/3/036802 (2017).
38. Wei, G. *et al*. Size-tunable Lateral Confinement in Monolayer Semiconductors. *Scientific Reports* **7**, 3324, https://doi.org/10.1038/s41598-017-03594-z (2017).
39. Nan, H. *et al*. Strong Photoluminescence Enhancement of MoS_2 through Defect Engineering and Oxygen Bonding. *ACS Nano* **8**, 5738–5745, https://doi.org/10.1021/nn500532f (2014).
40. Tongay, S. *et al*. Defects activated photoluminescence in two-dimensional semiconductors: interplay between bound, charged, and free excitons. *Sci. Rep.* **3**, 2657, https://doi.org/10.1038/srep02657 (2013).
41. Wang, F. *et al*. Tuning Coupling Behavior of Stacked Heterostructures Based on MoS_2, WS_2, and WSe_2. *Scientific Reports* **7**, 44712, https://doi.org/10.1038/srep44712 (2017).
42. Wu, H. *et al*. All-Inorganic Perovskite Quantum Dot-Monolayer MoS_2 Mixed-Dimensional van der Waals Heterostructure for Ultrasensitive Photodetector. *Advanced Science* **5**, 1801219, https://doi.org/10.1002/advs.201801219 (2018).
43. Gao, F. *et al*. Valley trion dynamics in monolayer $MoSe_2$. *Physical Review B* **94**, 245413, https://doi.org/10.1103/PhysRevB.94.245413 (2016).
44. Liu, W. *et al*. Carrier-density-dependent recombination dynamics of excitons and electron-hole plasma in-plane InGaN/GaN quantum wells. *Physical Review B* **94**, 195411, https://doi.org/10.1103/PhysRevB.94.195411 (2016).
45. Wang, H., Zhang, C. & Rana, F. Ultrafast Dynamics of Defect-Assisted Electron–Hole Recombination in Monolayer MoS_2. *Nano Letters* **15**, 339–345, https://doi.org/10.1021/nl503636c (2015).
46. Suh, J. *et al*. Doping against the Native Propensity of MoS_2: Degenerate Hole Doping by Cation Substitution. *Nano Letters* **14**, 6976–6982, https://doi.org/10.1021/nl503251h (2014).
47. Mohapatra, P. K., Deb, S., Singh, B. P., Vasa, P. & Dhar, S. Strictly monolayer large continuous MoS_2 films on diverse substrates and their luminescence properties. *Appl. Phys. Lett.* **108**, 042101, https://doi.org/10.1063/1.4940751 (2016).

Acknowledgements

We acknowledge the financial support from MEITY (Grant No. 5(9)/2012-NANO (VOL-II)) for carrying out part of this work. Central Instruments Facility, I.I.T. Guwahati is acknowledged for providing the Raman, TEM, and FESEM facilities.

Author contributions

The work was conceived by all three authors. L.P.L.M. and A.B. primarily conducted the experiments and analysis, and P.K.G. interpreted the results including theoretical modeling of the results. The manuscript was written and reviewed by all three authors.

Competing interests

The authors declare no competing interests.

Additional information

Supplementary information is available for this paper at https://doi.org/10.1038/s41598-019-55776-6.

Correspondence and requests for materials should be addressed to P.K.G.

Reprints and permissions information is available at www.nature.com/reprints.